

Far-infrared/millimetre Emission in 3C sources ^{*}

Dust in radio galaxies and quasars

Paola Andreani¹, Robert A. E. Fosbury², Ilse van Bemmél³, and Wolfram Freudling²

¹ Osservatorio Astronomico Padova, Vicolo dell'Osservatorio 5, Padova, I-35122, Italy ^{**} e-mail: andreani@mpg.de

² Space Telescope - European Coordinating Facility European Southern Observatory, Karl-Schwarzschild-Str. 2, D-85748 Garching bei München, Germany
e-mail: rfosbury@eso.org, wfreudli@eso.org

³ Kapteyn Astronomical Institute, P.O.Box 800, 9700 AV Groningen, The Netherlands e-mail: bemmel@astro.rug.nl

Received March, 2001; accepted

Abstract. We present far-infrared and millimetric observations of a sample of 3C objects. Millimetre data were taken at 1.25 mm with the IRAM 30m antenna feeding the MPIFR bolometer array. Mid-infrared (MIR) and far-infrared (FIR) photometry were carried out with the ISOCAM and ISOPHOT cameras on the ISO Satellite. Additional FIR IRAS observations are also included. We present the entire Spectral Energy Distributions (SEDs) from the UV to radio and discuss the emitting mechanisms. Two composite spectra, one for the radio galaxies and one for the radio quasars, are built in the object rest frame. While the SEDs of the two classes differ, they are indistinguishable in the MIR and FIR range where they probably arise as thermal emission from a dusty torus and a larger-scale (cooler) dust distribution in the host galaxy.

Key words. Galaxies: photometry, ISM - Quasars: general - ISM: dust - radio continuum: galaxies, ISM

1. Introduction

While classical papers on colours and luminosities of radio galaxies have explicitly ignored the presence of dust on the evidence of the strong Ly- α emission, blue colours and small scatter in the K-band Hubble diagram (Lilly & Longair 1984; Dunlop et al. 1989; Lilly 1989), more recent work adopts a more cautious approach and suggests that some of the observed properties can be interpreted as evidence for the presence of dust distributed on scales of tens of kpc. For instance, the detection of significant linear polarization in the UV/blue aligned light is identified with scattered light from a hidden AGN due to externally illuminated dust which acts as a very efficient reflector of UV light (di Serego Alighieri et al. 1989; Scarrott et al. 1990; Cimatti et al. 1993; di Serego Alighieri et al. 1996;

Cimatti & di Serego Alighieri 1995; Manzini & di Serego Alighieri 1996; Best & Longair 1999; Vernet et al. 2001).

Images taken with HST show evidence for dust lanes in a large fraction of 3CR galaxies with redshift $0.1 \leq z < 0.5$ and significant extinction is found in the central few kpc in some radio galaxies. Dust disc orientation is close to being perpendicular to the radio source axis and obscuration from dust may dominate the appearance of intermediate redshift sources, influence the apparent morphology of the optical galaxy and determine the alignment effect seen in powerful radio galaxies (Baum et al. 1995; de Koff et al. 1996; McCarthy et al. 1997; de Koff et al. 2000).

Furthermore, comparison of line strengths arising from the same ions and involving a common ground state with calculated line ratios provide a sensitive measure for reddening. Attempts were made to measure $\frac{Ly\alpha}{H\alpha}$ in a number of high- z radio galaxies and, in most of the cases, a significant amount of reddening (with $A_V > 0.3$) is found.

On purely theoretical grounds, one expects the production of significant amounts of dust at early epochs when galaxies were undergoing vigorous star formation. Thus

Send offprint requests to: P. Andreani

^{*} based on observations with ISO, an ESA project with instruments funded by ESA Member States (especially the PI countries: France, Germany, the Netherlands and the United Kingdom) with the participation of ISAS and NASA

^{**} *Present address:* Max-Planck I. für Extraterrestrische Physik, Postfach 1312, 85741 Garching, Germany

there is reason to believe that much of the UV luminosity of high redshift radio sources is reprocessed by dust. The question of whether there is indeed a large amount of dust associated with radio galaxies is important not only from the point of view of galaxy formation and evolution, but it can help us understand the apparent differences between radio galaxies and radio quasars and as a test for the Unification Scheme for AGN (van Bemmél, Barthel, de Graauw, 2000).

Direct emission from dust can be detected at FIR and sub-mm wavelengths where the thermal re-radiation from dust grains is expected. However, on the basis of IRAS data alone for quasars and radio galaxies, it is not straightforward to constrain the emission mechanism with great confidence and, in particular, the relative contribution of thermal and non-thermal components at FIR wavelengths can be addressed only in sources which are strongly lobe-dominated and therefore, supposedly, free of any observable beamed radiation (Heckman et al. 1992; Heckman et al. 1994; Hes et al. 1995; Hoekstra et al. 1997; van Bemmél et al. 2000). In these objects the radio axis is further away from our line of sight, and the beaming of non-thermal emission therefore less efficient. Thus if dust is present, one might see it in these objects.

The detection of HI absorption (Uson et al. 1991; Carilli et al. 1998) and CO emission has confirmed the existence of dense concentrations of both atomic and molecular gas in the nuclei of some radio galaxies and quasars and indicated that rich supplies of molecular gas may be ubiquitous in powerful radio objects detected by IRAS (Mirabel et al. 1989; Mazzarella et al. 1993; Evans et al. 1999; Evans et al. 2001).

Detection of sub-mm continuum (with JCMT at $850\mu\text{m}$ and with IRAM 30m at 1.25mm) in radio galaxies provides a picture in which sources with typical redshift $z < 1$ are, on average, not detected, while those at higher redshifts ($z > 2.4$) present strong sub-mm fluxes, suggesting the presence of spatially distributed dust with approximately $10^8 M_\odot$ in these objects (Chini & Krügel 1994; Dunlop et al. 1994; Ivison 1995; Best et al. 1998; Ivison et al. 1998; van der Werf 1998; Archibald et al. 2001). On the one hand, this could simply reflect a K-correction effect: the steep ($S \propto \nu^{3-4}$) slope of the dust-emitted spectrum producing an apparent constancy or increase of observed flux, at a fixed observed frequency, with redshift at constant luminosity. Alternatively, one could envisage an evolutionary effect with larger dust masses and luminosities at higher redshifts. In the latter case, the large FIR luminosities could be produced by large star-formation rates in extremely gas-rich galaxies, but it can be also due to a selection effect which favours the detection of those high- z objects with greater radio power (van der Werf 1998; Best et al. 1998).

At low-redshifts, the 3CR sample was the subject of extensive investigation at FIR wavelengths but the question of the presence of dust in these objects could not be settled on the basis of IRAS data alone.

Heckman et al. (1992,1994) claim that, if long wavelength FIR emission is due to thermal re-radiation by circumnuclear dust, quasars and radio galaxies are expected to show similar outputs of such radiation, because of the optical thinness of the thermal emission. But they show that 3C quasars are more powerful FIR ($60\mu\text{m}$) sources than 3C radio galaxies and this result can be used either to disprove the unification scheme of quasars and radio galaxies proposed by Barthel (1989), or to state that the FIR emission from quasars cannot be due to thermal re-radiation from dust unless the emitting region is very optically thick, resulting in some degree of radiated anisotropy (Pier & Krolik 1992; Granato & Danese 1996).

This issue was the subject of subsequent investigations. By computing the relative contributions from a relativistically-beamed core and isotropic emission at $60\mu\text{m}$, a significant beamed component from the nuclei of lobe-dominated quasars and radio galaxies *in addition* to the isotropic thermal dust component was found (Hes et al. 1995; Hoekstra et al. 1997). The infrared output of radio galaxies and even some quasars should also be affected by contributions from star-formation episodes (van Bemmél et al. 1998).

Deep integrations performed with the ISOPHOT camera on the ISO Satellite on a small sample of radio galaxies and quasars confirm the previously reported FIR excess in quasars (van Bemmél et al. 2000), with this excess extending up to restframe wavelengths of $\sim 130\mu\text{m}$. In their radio galaxies the relative contribution of dust at FIR wavelengths with respect to beamed emission was estimated to be 98% and emitted by cool dust. Meisenheimer et al. (2001) on the basis of 13 detections out of 20 ISOPHOT observations on 10 pairs of 3C radio galaxies and quasars do confirm the thermal nature of the infrared emission, but do not confirm the presence of an infrared excess in quasars.

We present in this paper ISO FIR and groundbased millimetric observations of a sample of 3C sources (see Sect. 2), containing both quasars and radio galaxies. We discuss the origins of the FIR-mm emission and the differences found between the two classes. Data are presented in Sect. 3 and the results are discussed in Sect. 4.

2. The sample selection

The sample discussed in the present work was selected from a larger sample which was proposed (proposal reference MRC-3CR) for observation with the ISOPHOT (Lemke et al. 1996) and, for a subset of sources, with the ISOCAM (Cesarsky et al. 1996) cameras on the ISO Satellite. The 3C sources were selected solely on the basis of their visibility with the ISO satellite in regions of low Galactic cirrus emission. No objects with $z < 0.3$ were included and the sample contained 50 sources classified as quasars and 85 as galaxies. The main purpose of the ISO proposal was an extensive study of the FIR emission mechanism in 3C sources and a comparative study of ra-

radio galaxies and quasars. These data, supplemented with millimetric observations, were to be used to disentangle radio synchrotron emission from the thermal dust emission. The assembled sample spans a large range of radio properties and cosmic look-back times to avoid the well known biases in high frequency selected samples that arise from relativistic beaming effects, while maintaining a statistically useful mix of radio galaxies and quasars. This strategy demands complete samples selected at low frequencies without any biases in spectral index, radio morphology or angular size. The 3CR sample is well suited for this problem within the redshift range that it spans ($z < 2$) and is still the only completely optically identified sample of low-frequency selected objects. This sampling frequency (178 MHz) does guarantee selection due to unbeamed, optically thin and thus isotropic, emission from the radio lobes and so avoids introducing any orientation bias.

After launch, the sensitivity of ISOPHOT proved to be inadequate to complete observations effectively in the time available. In the present work we discuss the observations taken with the IRAM 30m antenna, feeding the MPIfR bolometer array at 1.25 mm, of 27 of the 3C sources, selected purely on the basis of telescope visibility, from the original ISO proposal. We also present the ISOPHOT observations in the wavelength range 5–200 μm of 15 of them and ISOCAM observations of 10. Even though the original ISOPHOT observations were not completed, it is still possible to address some of the purposes of the proposal in a self-consistent way.

3. Observations

3.1. 1.25 mm data

The 1.25 mm data presented here were taken with the MPIfR 19-channel bolometer (Kreysa et al. 1998) at the focus of the IRAM 30m antenna (Pico Veleta, Spain) during March 1996 and March 1997. The filter set combined with the atmospheric transmission produces an effective wavelength around 1.25 mm; the beam size is $11''$ (FWHM) and the chop throw was set at $32''$ with a chopping frequency of 2 Hz. The average sensitivity for each channel, limited principally by atmospheric noise and measured before any sky-noise subtraction was $60 \text{ mJy}/\sqrt{\text{Hz}}$. The effect of the sky noise on flux measurements could, however, be substantially reduced by exploiting the correlation between signals from the different channels using the standard three beam (beam-switching + nodding) technique. The average rms value was 1 mJy for a typical integration time on-source of 2000 s.

Atmospheric transmission was monitored by making frequent skydips from which the derived zenith opacities were 0.09–0.3. Calibration was performed using Uranus as primary calibrator and Mars and Quasars from the IRAM pointing list as secondary sources. The different measurements vary by less than 5 % for both planets. If we include the uncertainty in the planet temperature, we estimate an

average flux calibration uncertainty of 10 %. Pointing was checked each hour and the average accuracy achieved was better than $3''$.

The data were reduced assuming that the target sources are unresolved, i.e., having an extent at mm wavelengths smaller than the size of the central channel. The other 18 channels (excluding one which suffered a large electronic loss) were then exploited to derive a low-noise sky estimate. The weighted average value of the sky, computed using these outer 17 channels, was subtracted from the signal in the central channel. Note that this procedure eliminates only that part of the sky fluctuation with correlation length smaller than the chop throw ($32''$), i.e., from fluid motions at *short* wavelengths. However, the dominant part of the atmospheric noise is produced by motions of convective shells on large scales (at *long* wavelengths) (Church, 1995), while high frequency (5–20 Hz) fluctuations do not contribute significantly to the noise and are averaged over 0.25 s per phase, while the wobbling of the secondary smooths out the low frequency noise. According to Andreani et al. (1990), the correlation length for convective shells at these wavelengths is of the order of several tens of centimeters, i.e., only fluctuations generated at an altitude greater than 2000m above the telescope survive the double-switching subtraction and contribute to the noise. At altitudes greater than 5000m above sea level, however, the residual water vapour is very low and contributes little to the noise.

1.25 mm fluxes with the associated 1σ uncertainties are given in table 1. The first uncertainty is statistical while the second one derives from the calibration uncertainty related to the planetary measurements and their temperature uncertainty. Our 1.25 mm fluxes towards 3C 286, 3C 309.1, 3C 295 and 3C 325 differ slightly from those reported by Meisenheimer et al. (2001). They agree, however, within the calibration uncertainties.

3.2. IRAS and radio data

The IRAS data are taken from co-added survey data provided by IPAC and based on the SCANPI (Scan Processing and Integration Tool) processor. This procedure computes the one-dimensional co-addition of all the IRAS survey data of the source. The sensitivity is comparable to that achieved by the FSC (Faint Source Catalog) for point sources (see the IPAC manual for details). The resulting fluxes are listed in table 2. We have also applied the SUPERSCANPI procedure, which is similar to SCANPI but allows the inference of an average value of the FIR emission of the whole class of object. By dividing our sample into two separate classes, radio galaxies and quasars, we have applied the SUPERSCANPI procedure to estimate the weighted-average fluxes at 12, 25, 60 and 100 μm separately for each. These values are listed in table 2. The same procedure, but applied to a much larger set of objects, was used by Heckman et al. (1992). Within our larger uncertainties our results for radio galaxies and

quasars are in agreement. For 3C 268.3 IRAS data were taken from Hoekstra et al. (1997). Radio data are taken from NED (NASA Extragalactic Database).

3.3. ISO data

Fifteen objects of the present sample were observed with the ISOPHOT camera. For two objects, 3C 268.4 and 3C 280, data were collected for our programme (RFOSBURY MRC-3CR2) on July 3rd 1996, at 60 and 90 μm . Data for 3C 295, 3C 309.1, 3C 325 and additional observations of 3C 280 were taken from 5 to 170 μm , those of 3C 286, 3C 287 from 5 to 100 μm by Chini and have been independently published by Meisenheimer et al. (2001). These data together with those of 3C 268.4 (at 90 and 170 μm) 3C 313 (90 μm), 3C 288.1 (25-170 μm), 3C 352 and 3C 356 (90 and 160 μm) were taken from the archive and reduced by us with the Phot Interactive Analysis tool (PIA) version 8.0 (Gabriel et al. 1998). All data were taken in chopping mode except those for 3C 352 and 3C 356 which were mapped in raster mode. These latter data were reduced as described in van Bemmell et al. (2000). Data for 3C 46, 3C 268.3, 3C 295, 3C 337 and 3C 343.1 are taken from Fanti et al. (2000) and that paper, in which there is an extensive discussion, should be consulted for any details concerning the observing procedure and the data reduction.

Our analysis of the ISO data of the sources 3C 286, 3C 287, 3C 295, 3C 309.1, 3C 325 agree within the error bars with that by Meisenheimer et al. (2001) but clear detections towards 3C 280 were obtained because of the different observational setup with much longer exposure time.

Our reduction procedure is briefly summarized as follows:

- Ramps (V/s) of the Edited Raw Data (ERD) are linearized and cosmic hits are removed using the two-threshold deglitching procedure. A linear fit is then applied to the ramps providing the Signal per Ramp Data (SRD).
- All the data corresponding to one chopper position are then averaged and extrapolated in time to a value of constant detector response (*Pattern Analysis*).
- To correct the remaining cosmic hits, another deglitching procedure is applied. All the ramp signals per raster point are averaged and data are then processed to Signal per Chopper Plateau (SCP) level.
- Data are then corrected for reset interval and dark current is subtracted. A signal linearization which corrects for a changing response during the measurements is then applied.
- The same procedure is applied to the Fine Calibration Source (FSC) data to provide the internal calibration data.
- Source signal is estimated by subtracting the background. This latter is determined by averaging the sig-

nals corresponding to off-source positions of the chopper.

The resulting fluxes are listed in table 3. Note that for 3C 352 and 3C 356, although our analysis shows a signal-to-noise ratio larger than 7 at 160 μm and larger than 5 at 90 μm , respectively, a good estimate of the flux levels cannot be achieved because of excessively noisy FSC data, which prevent us from performing a good internal calibration.

3.4. ISOCAM data

ISOCAM observations were taken towards 3C 288.1, 3C 295, 3C 305, 3C 309.1, 3C 343.0, 3C 343.1, 3C 345, 3C 352 and 3C 356. These ISOCAM observations together with other radio galaxies and data reductions will be published elsewhere (Siebenmorgen & Freudling, 2001, in preparation). A complete ISOCAM catalogue was built by these authors. They have reduced staring and raster observations of 3C sources in the ISOCAM archive using a homogeneous procedure. The procedure was optimized for faint sources, and particular effort was taken to effectively remove ‘glitches’ in the data. Aperture Photometry was carried out on all sources using two independent procedures for background estimates and weighting. We address the reader to that paper for all further details.

3.5. UV, optical, near-IR and sub-mm data

Optical and UV and near IR photometry are taken from Best et al. (1998) deVries et al. (1998) and deKoff et al. (1996). Two objects, 3C 322 and 3C 356 were observed with SCUBA at 450 and 850 μm by Archibald et al. (2001).

4. The Spectral Energy Distribution of Radio Galaxies

Figs 1–3 show the spectral energy distribution from UV to radio wavelengths of the sample sources. 17 out of 27 objects were detected in the MIR and/or in the FIR. We consider as reliable detections all the MID and FIR fluxes with $\frac{S}{N} \geq 5$, and as marginal detections those with lower $\frac{S}{N}$ ratio ($3 < \frac{S}{N} < 5$).

4.1. Radio spectrum

We first consider the radio region of the SED. There is no way to constrain uniquely the non-thermal radio spectrum unless high-frequency ($\nu > 15$ GHz) radio data are available. A break frequency, depending on the magnetic field, for a synchrotron spectrum is expected at high frequencies because of electrons cooling. The amount of steepening cannot be estimated with the present data since most of the sources were not observed in the frequency range between 5 GHz and 240 GHz (1.25 mm) and only one third have data at 15 GHz. It is, therefore, not possible to reliably extrapolate the radio data at higher frequency to

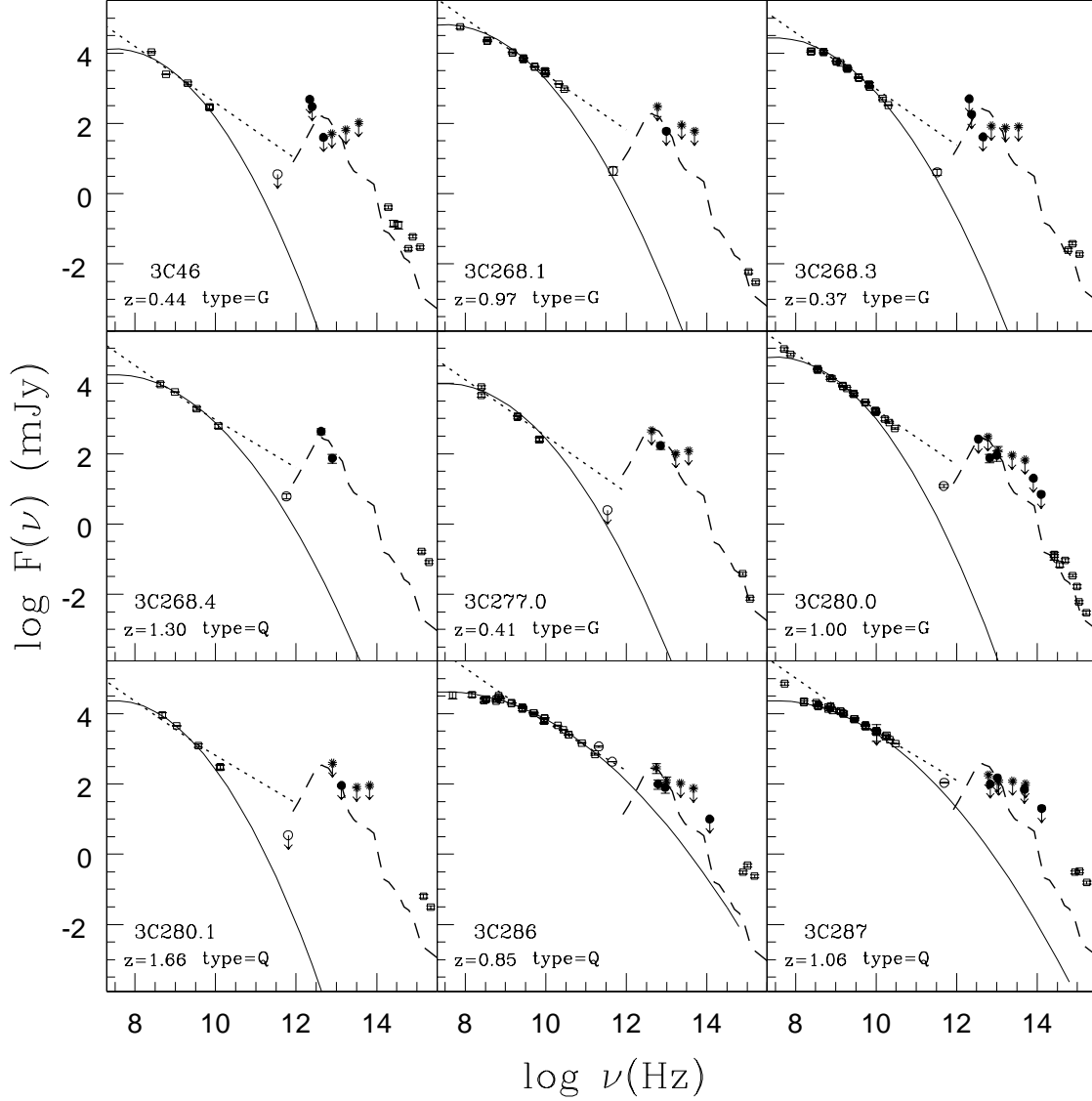


Fig. 1. Spectral Energy Distributions (SEDs) from radio to UV wavelengths. mm points are shown as open circles, ISO data as filled circles, IRAS points at 12, 25, 60 and $100\,\mu\text{m}$ are shown as asterisks, radio and optical observations as open squares. For fluxes with signal-to-noise ratios, $\frac{S}{N} \leq 3$ a 3σ upper limit is shown as a down-arrow. Two simple approximations of the non-thermal emission spectra are shown through the radio data: the solid curve corresponds to equation 2 while short-dashed lines to the classical power-laws with spectral index of $\alpha_{rg} = -1.04$ for radio galaxies and $\alpha_{qs} = -0.91$ for quasars. The long-dashed curve is the output from a model whose basic prescription is the reprocessing by ISM dust of the UV-optical light (see text for details).

disentangle any thermal contribution from the 240 GHz flux and infer or reject the presence of another component contributing to the mm emission. For the 17 objects detected in the FIR, it is possible to combine the FIR data with the mm point and try to estimate the two likely contributors — thermal and non-thermal.

In what follows, we make two different assumptions. First we assume that the sources are all sufficiently old that the turn-over frequency is low. In this case, most of the electrons have lost their energy since there is no mech-

anism to continuously produce and/or accelerate them. We only fit points at frequencies above the turn-over (assumed to be at 178 MHz) with the usual power-law of synchrotron emission $F \propto \nu^\alpha$. We take as α the average values for 3C radio galaxies and quasars, i.e. $\alpha_{rg} = 1.04$ $\alpha_{qso} = 0.91$ found by (Heckman et al. 1992) in the frequency range 1.4–15 GHz. We then assume that the synchrotron spectrum between a few GHz and hundreds of GHz maintains the same slope and we extrapolate it to mm wavelengths. Any difference between the predicted

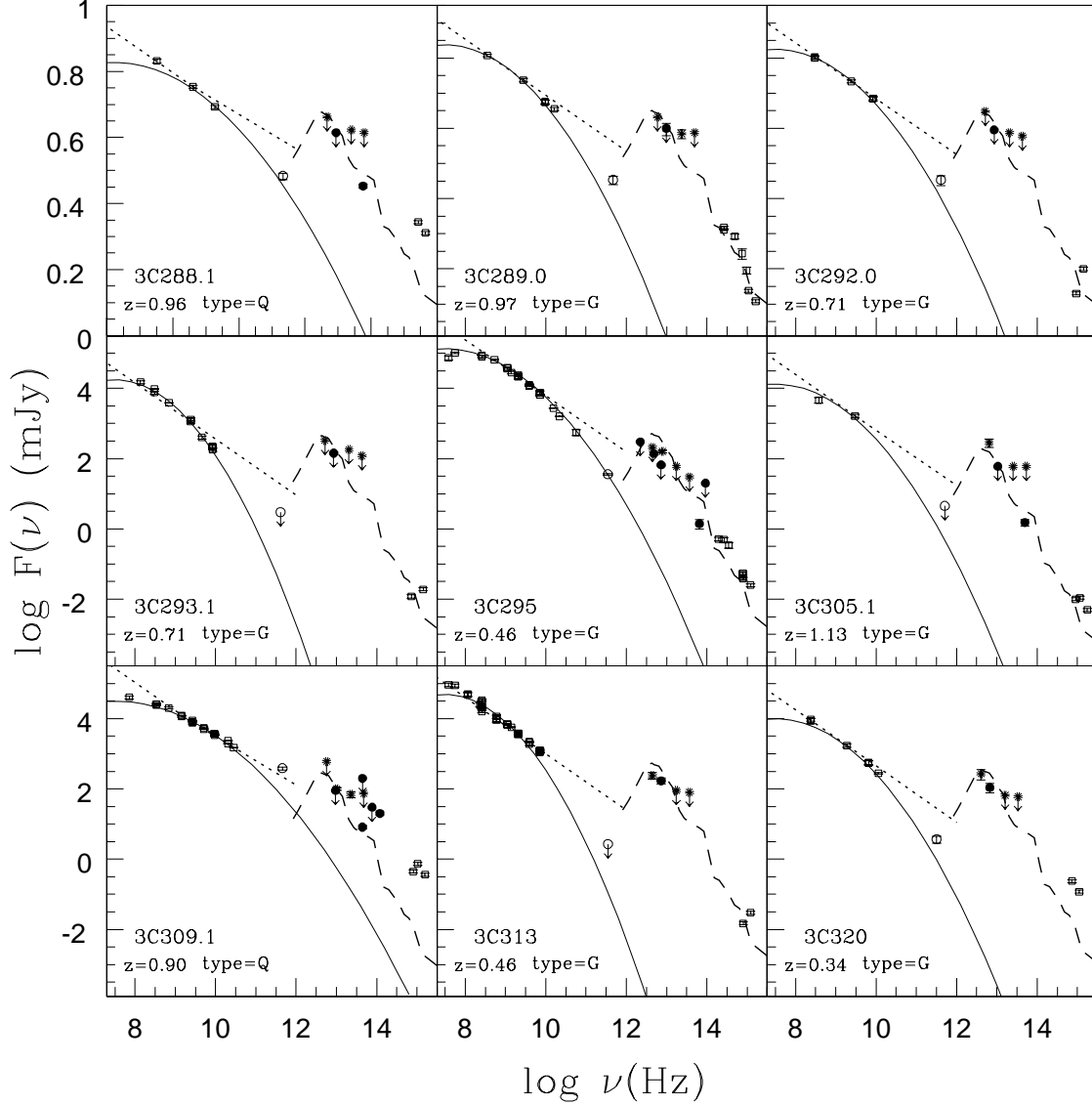


Fig. 2. same as figure 1

and observed values at 240 GHz is attributed to an additional spectral component.

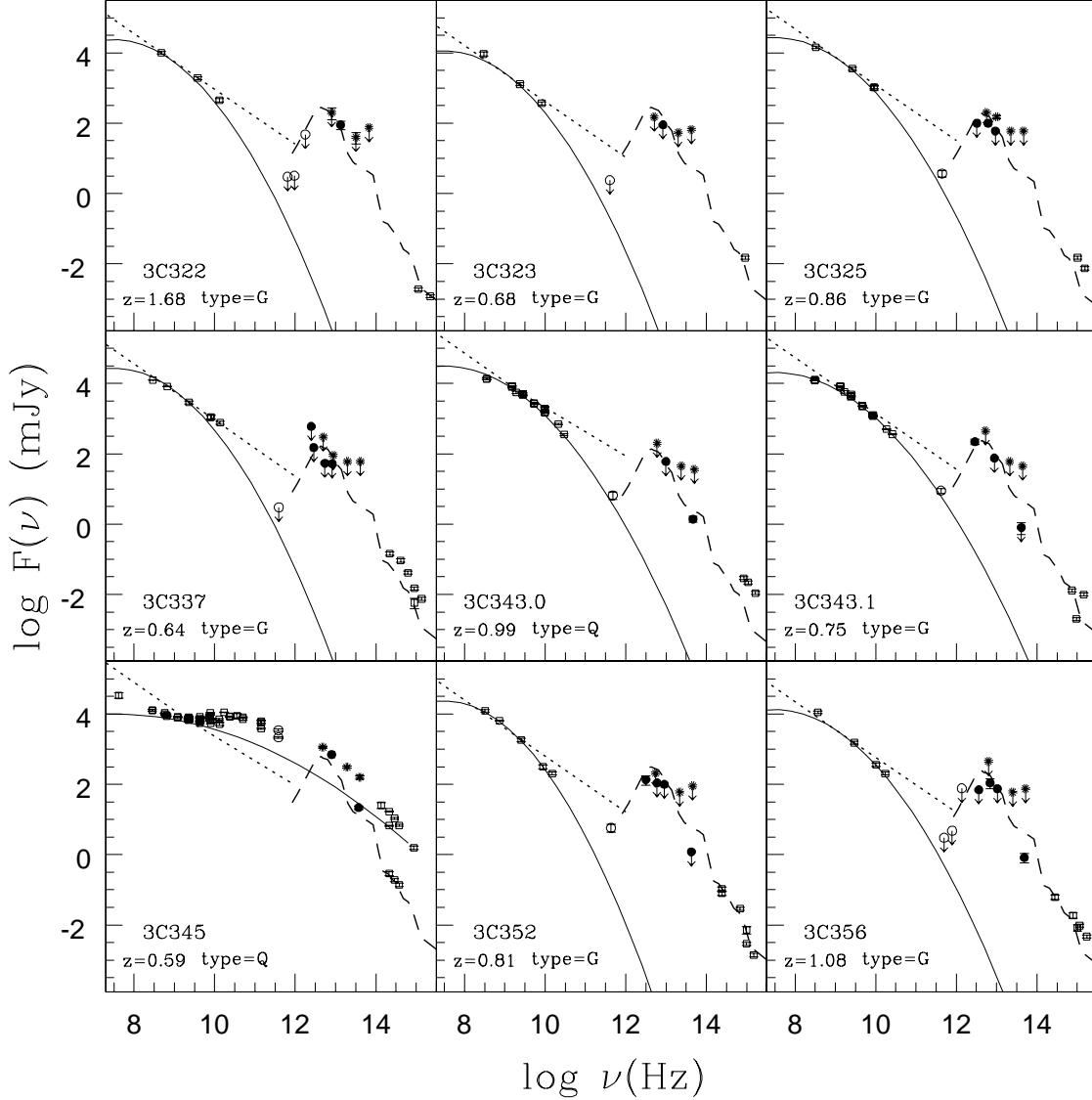
This simple approximation provides a poor match to the whole radio spectrum, low and high frequency radio data lie above and/or below the expected power-law. In particular, the *mm emission for all radio galaxies and the three quasars 3C268.4, 3C280.1, 3C343.1* lies well below this extrapolation (see also van Bemmél & Bertoldi, 2001). It must be stressed here that the 1.25 mm observations only refer to the flux emitted by the source within the central 11". If the radio-lobes dominate the radio spectrum and have a larger extent, it is possible that some 1.25 mm flux is lost in our observations. This could be true for the giant radio galaxies 3C277 and for 3C356. For all the other objects, which have a more compact morphology, the further steepening of the spectrum is real.

At present the contribution from radio-lobes to the mm flux it is not observationally settled. For instance, van Bemmél and Bertoldi (2001) do not detect any difference in radio-millimetre SED of large and small objects and suggest that at least in their objects is the core dominating the millimetre emission.

More generally, a self-absorbed synchrotron emission spectrum with an electron power-law energy distribution $N(E) \propto E^{-s}$, can be parameterised as follows (see e.g. Polletta et al. 2000):

$$L_\nu \propto \left(\frac{\nu}{\nu_t}\right)^{\alpha_1} \left\{1 - \exp\left(-\left(\frac{\nu}{\nu_t}\right)^{\alpha_1 - \alpha_2}\right)\right\} e^{-\frac{\nu}{\nu_c}} \quad (1)$$

where α_1 and α_2 are the spectral indices for the optical thick and thin cases respectively ($\alpha_1 = 2.5$ and $\alpha_2 = -(s-1)/2$ for a homogeneous source), ν_t is the frequency at which the plasma optical depth reaches unity

Fig. 3. same as figure 1

and ν_c is the cut-off energy of the plasma energy distribution. For frequencies lower than ν_t and by neglecting the high-energy cut-off, ν_c – which although depending on the assumed electron energy and the source magnetic field for relativistic electron and a Galactic magnetic field it is higher than a few hundreds GHz – this expression can be approximated by a parabola-shaped curve in a log-log plane:

$$\log F_\nu = C + \frac{1}{2A}(\log \nu - \log \nu_t)^2 \quad (2)$$

where $\frac{1}{A} = 2\alpha_1 - \alpha_2$. We then use this latter expression to fit all the radio data with $\nu \leq 240$ GHz where ν_t is taken equal for all sources, 31.6 MHz. The free parameters are C , the normalization factor, and A representing the bending of the curve whose best-fit value varies between -0.2 and -0.55. For those objects with more than 4 points

at frequencies lower than 240 GHz a minimizing- χ^2 fit was carried out, while for those sources with fewer than 4 radio points the fit is not statistically significant and must be considered only as indicative.

These parabola-shaped curves are shown in Figs. 1–3 as a solid line, while the power-law curve is shown as short-dashed.

For 3C 268.3, 286, 293.1, 295, 343, 343.1 a parabola-shaped non-thermal spectrum fits well the entire radio spectrum up to 240 GHz. Again we stress here that in most cases and in particular for these objects the 240 GHz point undoubtedly shows that the radio spectrum bends at high energy. However, it is difficult to disentangle from the mm data any residual emission not related to the synchrotron one but to a thermal cool dust component. Even for those objects with well sampled radio spectrum only the combination of mm with FIR data allows the infer-

ence of a different emitting mechanisms on a more solid basis.

3C 286, 287, 309.1 and 345 have a very large mm flux. The overall spectrum from radio to optical wavelengths could be interpreted as due to a dominant non-thermal component. As expected, it is not possible to fit the entire spectrum with a single component, as shown in Figs 1–3. It is likely that the electrons population does not have a single age for the entire source. Furthermore, variability plays a role at least for 3C 345. Even for 3C 286 and 3C 309.1 with FIR detections it is tough to infer any additional, most likely thermal, component from cold dust contributing to the mm flux.

4.2. FIR and optical spectrum

For wavelengths $\lambda < 200\mu\text{m}$, the interpretation of the observed SED is not straightforward since both stars and AGN, each with their associated dust obscuration and emission, must be taken into account. To effectively constrain all these components requires high quality data between 3 and $300\mu\text{m}$ in addition to those in the NIR-optical range. Existing observations allow the construction of useful SED for thirteen sources with FIR data: 3C 280 (IRAS/ISO), 3C 286 (ISO), 3C 288.1 (ISO), 3C 289 (IRAS), 3C 295 (ISO), 3C 305 (ISO), 3C 309.1 (ISO/IRAS), 3C 322 (IRAS), 3C 325 (ISO), 3C 343.1 (ISO), 3C 345 (IRAS/ISO), 3C 352 (ISO) and 3C 356 which have reliable measurements in this range.

Although the number of data available for most of the sources is small, we use them to compare the observed SED from the optical to 1 mm with the model developed by Mazzei and De Zotti (1996) for radio galaxies. They have constructed a spectrophotometric population synthesis model incorporating dust extinction and re-emission and a non-thermal central source which successfully reproduces the SEDs of high- z radio galaxies.

No attempt is made to *fit* this model to the radio galaxies data. We do, however, plot it in Figs 1–3, arbitrarily normalized at the $60\mu\text{m}$ flux (or upper limit). In particular this spectrum was used to reproduce the radio galaxy SEDs where the *scattered* AGN component dominates the UV rest frame light and the old stellar population of the host galaxy is the major contribution at longer wavelengths. The dust reprocessed starburst light dominates the spectrum at long wavelengths ($\lambda > 10\mu\text{m}$), while the reprocessing of AGN energy is negligible. This is consistent with the model in Vernet et al. (2001) for the $z \sim 2.5$ radio galaxy, 4C+48.48.

Note that the shape of the predicted spectrum agrees quite well with the observed behavior of the radio galaxies UV-optical-IR SED, in particular for 3C 280, 3C 289, 3C 295, 3C 305, 3C 322, 3C 343.1, 3C 352 and 3C 356. Quasars, on the other hand, have a different UV-optical spectrum, brighter by one dex and dominated by the AGN component.

4.3. The composite spectra

To better address the relative importance of the different components in radio galaxies and quasars, their composite spectra were built and are shown in Fig. 4. The sample was split into two: radio galaxies and quasars. 3C 345 was not included in the latter class because of its extreme variability. In order to compare spectra of sources at different distances data were normalized to the $60\mu\text{m}$ flux. The frequency range is divided into bins in the object rest-frame and the $60\mu\text{m}$ -normalized data are (weighted) averaged in each bin and errors are given by the dispersion around the average. When censored (upper limit) data are present, the Kaplan-Meier estimator was used to estimate the average values and their errors (Feigelson 1990; LaValley et al. 1992). Here we would like to point out the limits of this analysis. It could be argued that the mid-far-IR spectra of QSOs do not form a very homogenous classes and on the basis of the present data alone there seem indeed to be a difference between 268.4, 280.1, 288.1, 343.0, on the one hand, and 286, 287, 309, 345, on the other hand, we feel however that it is premature to argue for a qualitative difference, because of the poor sampling of the spectra of the former objects, and we continue to consider the QSO class as a whole.

Inspection of Fig. 4 allows us to infer the following:

- The two classes of object show a similar radio spectral shape up to a frequency of around 300 MHz.
- For $\nu > 300$ MHz the quasars spectrum is elevated by a factor larger than 3 up to 240 GHz (1.25 mm), which is most likely to be due to a non-thermal, beamed component (van Bemmél & Bertoldi 2001).
- The sharp turn-over of the radio spectrum excludes a significant contribution of the non-thermal component to the FIR fluxes for the radio galaxies and half of the quasars studied in this work.
- No evident difference is detected in the FIR part of the spectrum from $100\mu\text{m}$ to 1 mm . This result is satisfactorily in agreement with the fact that the emission has a thermal origin, very likely linked to the concurrent Starburst in the galaxy disc. This is consistent with the result of previous studies (Polletta et al. 2000).
- The optical and UV part of the spectrum differs by one dex or more between the two classes.

In the framework of Unified Scheme of AGN this result is not unexpected since the difference between the two classes is only an orientation-dependent effect. An inspection of Fig. 4, together with results from independent observations, seems to support this picture: (a) the dusty torus emits between 10 and $50\mu\text{m}$ and heated by the AGN, (b) an additional cool component emitting at $100\text{--}140\mu\text{m}$ and representing the reprocessed stellar energy in the host environment is clearly seen in radio galaxies and it may be outshone by the stronger non-thermal beamed component in quasars, (c) the difference at UV-optical wavelengths between the two classes is due to the obscuration of the AGN in the radio galaxies by the optically thick torus.

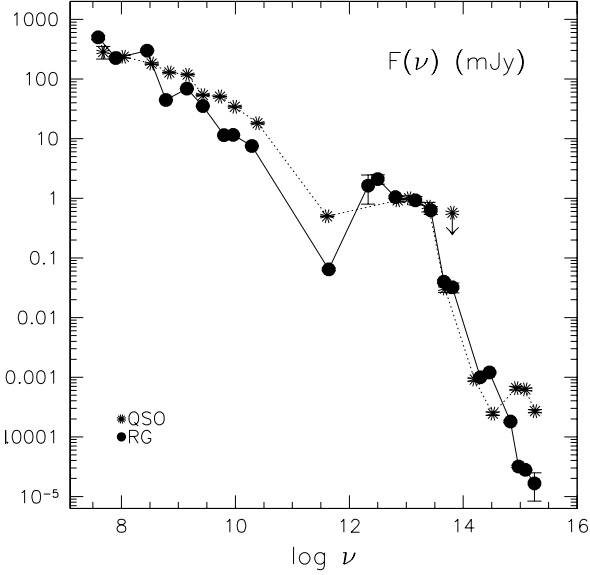


Fig. 4. The composite spectra of 3C quasars and 3C radio galaxies in our sample. quasars points are shown as asterisks, while radio galaxies points as filled circles. Data are averaged in each wavelength bin in the object's rest-frame (see text for details). Error bars are in general smaller than the points size except at $\log \nu = 12.3$ ($150 \mu\text{m}$) and at $\log \nu = 15.25$ ($0.17 \mu\text{m}$).

The optical/UV flux which remains visible in these objects can be a combination of scattered AGN light and a direct view of a young stellar population (Vernet et al. 2001).

5. A colour-magnitude diagram for radio galaxies

Before analysing flux ratios we show in Fig. 5 1.25 mm and $60 \mu\text{m}$ fluxes against the source redshift. Both detection and upper limits are equally distributed in redshift and do not show any clear trend with z .

Fig. 6 shows the ratio between the 1.25 mm and the $60 \mu\text{m}$ fluxes, $\frac{F_{1\text{mm}}}{F_{60\mu\text{m}}}$, against the source redshift. $60 \mu\text{m}$ was chosen since it is the most common measured wavelength amongst our objects. Asterisks refer to quasars and filled circles to radio galaxies. The values for those sources with upper limits at both wavelengths (3C 46, 3C 280.1, 3C 293.1, 3C 305.1, 3C 323, 3C 337) are identified as open circles and plotted at the positions of these limits. Upper limits are given for those objects detected at $60 \mu\text{m}$ but not at 1 mm (3C 356, 3C 277, 3C 313, 3C 322) and lower limits for 3C 268.1, 3C 268.3, 3C 287, 3C 292, 3C 343, 3C 343.1, 3C 288.1 3C 320, detected at 1 mm but not in the FIR. Note that there is no redshift-dependence of the detection rate at either wavelength. The average value of $\frac{F_{1\text{mm}}}{F_{60\mu\text{m}}}$ for the radio galaxies class is around 0.05 while for quasars, it is one order of magnitude higher as seen directly from the relative SEDs (Figs 1 through 4). A bimodal distribution appears in Fig. 6 where objects whose SED is dominated by the non-thermal emission lie in the

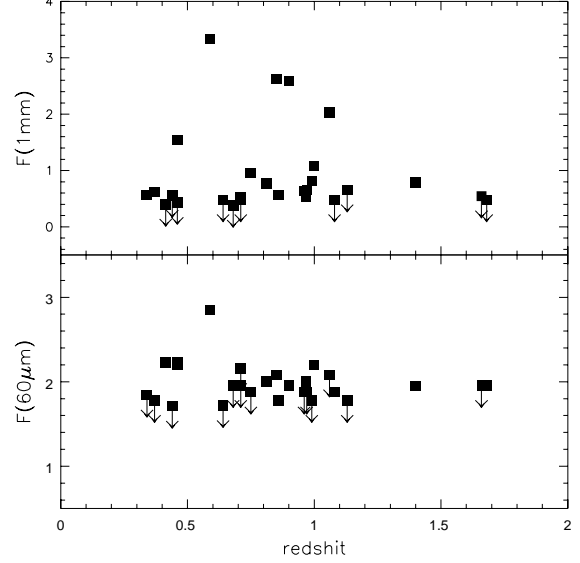


Fig. 5. Upper panel reports the 1.25 mm fluxes, lower panel those at $60 \mu\text{m}$ against the source redshift. Down arrows correspond to upper limits.

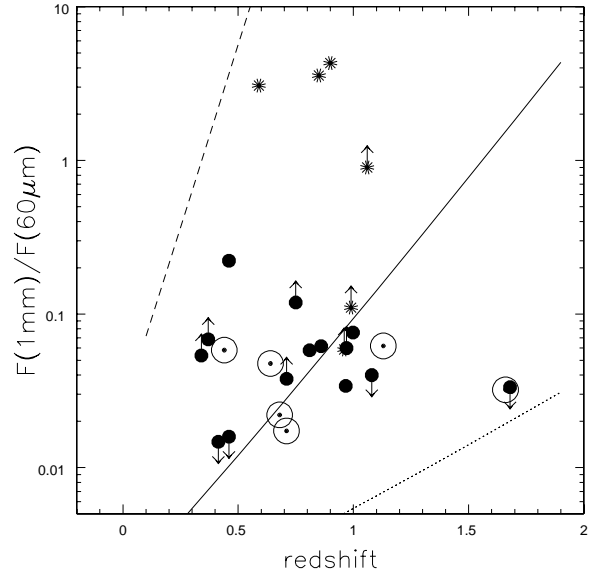


Fig. 6. The ratio $\frac{F_{1\text{mm}}}{F_{60\mu\text{m}}}$, is shown against the source redshift. Filled circles are radio galaxies, asterisks quasars. Open circles correspond to objects not detected at either wavelength. Variation with z of the ratio for a thermal spectrum, $\epsilon(\lambda) \cdot B(\lambda, T_d)$, with $T_d = 50 \text{ K}$ and $\epsilon \propto \lambda^{1.5}$ (where ϵ is the wavelength-dependent dust emissivity) is represented by a solid line $T_d = 100 \text{ K}$ by the dotted line and $T_d = 20 \text{ K}$ by the dashed line.

upper part of the plot. In those objects it is likely that any thermal mm emission is overwhelmed by the synchrotron components.

The lower part of the plot contains those sources for which the thermal component starts to dominate even at

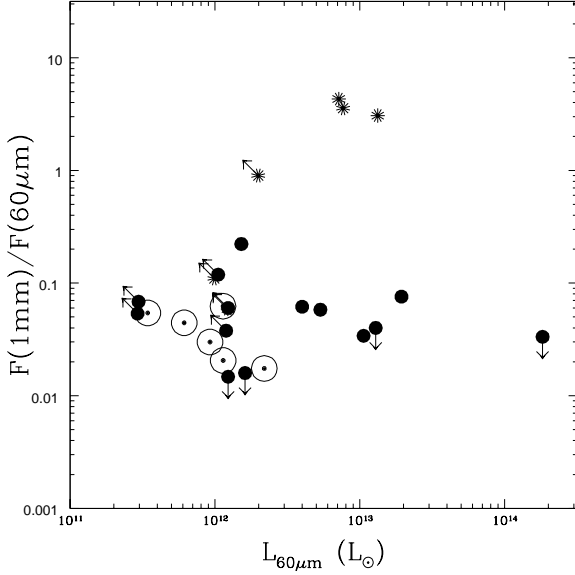


Fig. 7. The ratio $\frac{F_{1.25\text{mm}}}{F_{60\mu\text{m}}}$, is plotted against the source 60 μm luminosity. Filled circles are radio galaxies, asterisks quasars. Open circles correspond to objects detected at neither wavelength.

mm wavelengths. Some of the objects distribute themselves along a line corresponding to a thermal spectrum with a dust mean temperature of 50 K at different redshifts. Objects like 3C 295, 3C 268.3, 3C 320 and 3C 343.1 fall to the left of the plot because of a lower temperature dust component or to a higher non-thermal component, while 3C 322, which lies in the lower-right corner could have a different thermal spectrum with a hotter average dust temperature (around 100 K). This is indeed supported by the non-detection of this object in the SCUBA photometry at 450 and 850 μm (Archibald et al., 2001).

To further investigate the ratio between the 1.25 mm and the 60 μm fluxes, $\frac{F_{1.25\text{mm}}}{F_{60\mu\text{m}}}$, and make it distance-independent in Fig. 7 $\frac{F_{1.25\text{mm}}}{F_{60\mu\text{m}}}$ is plotted against the 60 μm rest-frame luminosity, $L_{60\mu\text{m}}$, for all the sources in our sample. The luminosity is computed in an Einstein-de Sitter Cosmology with $\Omega = 1$ and $H_0 = 65\text{km/s/Mpc}$ and using a K-corrected thermal spectrum with dust emissivity index of $\beta = 1.5$.

While the conclusions drawn from this plot should be regarded as tentative, the shifting of lower limits, towards the left along the x-axis and upwards along the y-axis, as indicated by the arrows would not change the observed trends. In this figure, the radio galaxies are located preferentially along a sequence of slightly decreasing $\frac{F_{1.25\text{mm}}}{F_{60\mu\text{m}}}$ for increasing $L_{60\mu\text{m}}$, while half of the quasars show much larger $\frac{F_{1.25\text{mm}}}{F_{60\mu\text{m}}}$ values.

The diagram suggests some interesting conclusions. Half of the quasars share the common properties of the radio galaxies, while the other half show large $\frac{F_{1.25\text{mm}}}{F_{60\mu\text{m}}}$ ratios. This can be explained if these latter quasars have a dominant non-thermal spectrum, possibly the beamed

component much stronger than that observed for those objects on the lower-left part of the diagramme. Low value of the ratio $\frac{F_{1.25\text{mm}}}{F_{60\mu\text{m}}}$ can be due to the presence of cool dust. Most of radio galaxies fall in the region where ($\frac{F_{1.25\text{mm}}}{F_{60\mu\text{m}}}$, $L_{60\mu\text{m}}$) is consistent with the expected behavior of a thermal spectrum with temperatures ranging between $T=20\text{K}$ and $T=50\text{K}$. Four objects, 280, 356, 289 and 322, lying to the right in the plot, could be characterized by a higher dust temperature. Indeed the ratio $\frac{F_{1.25\text{mm}}}{F_{60\mu\text{m}}}$ for a thermal spectrum with temperature increasing from $T=20\text{ K}$ to $T=200\text{ K}$ at $z = 0.5$ and $z = 1.5$ (roughly the redshift range of the present sample) decreases as the 60 μm luminosity increases.

6. Conclusions

The investigations of the entire spectral energy distributions of a small sample of 3C sources with mm and FIR observations allows us to draw the following conclusions:

1. Detected fluxes and upper limits at 60 μm and 1.25 mm are equally distributed in redshift and do not show any trend with z . This result is true also for all the ISO detections.
2. The average power-law spectrum through the radio data, with spectral indices taken from other studies on quasars and radio galaxies (Heckman et al., 1992), shows that for most of the objects the mm point lies below the extrapolation of this law to 240 GHz (1.25 mm). This means that the radio spectrum bends at frequencies lower than 240 GHz. In some of the mm-detected objects different spectral components could contribute to the detected fluxes. The origin of the mm emission in these objects is mainly non-thermal for flat-spectrum sources. In some sources there could be an additional thermal component from cool dust, but without sampling the submm region of their spectrum this component still remains elusive.
3. QSOs have much stronger mm emission. For half of them, the entire SEDs from radio to UV wavelengths can be due to the superposition of different non-thermal components arising from either self-absorbed synchrotron and/or synchrotron emission from a hard electron spectrum. However for the remaining quasars, the ratio $\frac{F_{1.25\text{mm}}}{F_{60\mu\text{m}}}$ is similar to that of radio galaxies, implying a common origin of the mm-FIR emission.
4. Composite spectra for radio galaxies and quasars have been constructed in the object restframe: the main differences are seen in radio - mm and optical SEDs, while the FIR SEDs are remarkably similar. This points to a common origin of the FIR emission which is likely to be dust-reprocessed energy from star formation in the host galaxy and/or with a contribution from the dusty AGN-torus. Although on the basis of these data alone we cannot fully address this issue in quasars, the far-IR detections in quasars suggests that

there is a thermal as well as a powerful non-thermal component in these objects.

5. The similarity of the FIR SED of the two populations is consistent with the predictions of the orientation-based unified scheme and suggests the presence of dust either encircling the AGN or in the body of the host galaxy or both. On the basis of these data alone it is not possible to identify the main heating mechanism — AGN or star-formation — though the presence of cool dust emission, the width of the FIR spectrum and modeling suggest that, at least in radio galaxies, dust — which could extend to large distances from the heating source — is the main FIR emitter.

Acknowledgements. P.A. acknowledges support from the Alexander von Humboldt Foundation and thanks MPE for hospitality. RAEF is affiliated to the Astrophysics Division of the Space Science Department, European Space Agency.

Part of the data used in this work were taken with the SCANPI procedure, developed by the NASA Archival center for IRAS Satellite (IPAC) operating by JPL and made use of the ASURV package Rev 1.2 kindly provided by E. Feigelson. This study has made use of the NASA/IPAC Extragalactic Database (NED) and was partially supported by ASI (Italian Space Agency) under contract ARS-98-226 *Astrofisica di sorgenti X e gamma compatte*. We also thank an anonymous referee for his comments helped in improving this paper.

References

- Andreani P., Dall'Oglio G., Martinis L., Piccirillo L., Pizzo L., Rossi L., 1990 *Infr. Phys.* 30, 479
- Archibald E.N., Dunlop J.S., Hughes D.H., Rawlings S., Eales S.A., 2001, *MNRAS* 323, 417
- Barthel P., 1989, *ApJ* 336, 606
- Baum S.A. et al. 1995, in *Cold Dust at High Redshift*, Hoogeveen, the Netherlands, eds Bremer M.N., van der Werf P.P., Röttgering H.J.A.
- Best P.N. & Longair M., 1999 in *The Most Distant Radio Galaxies*, Proceedings of the colloquium, Amsterdam, 15-17 October 1997, Royal Netherlands Academy of Arts and Sciences. Eds H. J. A. Röttgering, P. N. Best, and M. D. Lehnert., p. 59.
- Best P.N. et al. 1998, *MNRAS* 301, L15
- Carilli C.L., Menten K.M., Reid M. J., Rupen M.P., Yun M.S., 1998, *ApJ* 494, 175
- Cesarsky C., et al. , 1996 *A&A* 315,
- Chini R. and Krügel E., 1994, *A&A* 288, 33
- Church S.E., 1995, *MNRAS* 272, 551
- Cimatti A., di Serego Alighieri S., Fosbury R.A.E., Salvati M. and Taylor D., 1993, *MNRAS* 264, 421
- Cimatti A. & di Serego Alighieri S. 1995, *MNRAS* 273, L7
- de Koff S., Baum S.A., Sparks W.B., Biretta J., Golombek D., Macchetto F., McCarthy P., Miley G. K. 1996, *A&AS* 107, 621
- de Koff S., Best P., Baum S.A., Sparks W.B., Röttgering H., Miley G., Golombek D., Macchetto F., Martel A., 2000, *A&AS* 129, 33
- de Vries W.H., O'Dea C.P., Baum S.A., Perlman E., Lehnert M.D., Barthel P.D., 1998, *ApJ* 503, 156
- di Serego Alighieri S., Fosbury R.A.E., Quinn P.J. and Tadhunter C.N., 1989 *Nat* 341, 307
- di Serego Alighieri S., Cimatti A., Fosbury R.A.E., Perez-Fournon I. 1996, *MNRAS* 279, L57
- Dunlop J.S., Guiderdoni B., Rocca-Volmerange B., Peacock J., Longair M. 1989, *MNRAS* 240, 257
- Dunlop J.S., Hughes D.H., Rawlings S., Eales S.A., Ward M.J., 1994 *Nat* 370, 347
- Evans A.S., Sanders D.B., Surace J.A., Mazzarella J.M., 1999, *ApJ* 511, 730
- Evans A.S., Frayer D.T., Surace J.A., Sanders D.B., 2001, *AJ* 121, 1893
- Fanti C. et al. 2000, *A&A* 358, 499
- Feigelson, E. D. "Censored Data in Astronomy", *Errors, Bias and Uncertainties in Astronomy*, eds. C. Jaschek and F. Murtagh, (Cambridge U. Press: Cambridge) p. 213 1990.
- Gabriel C., Acosta-Pulido J., Heinrichsen I., 1998, Proc. ADASS VII, ASP Conf. Ser. 145, eds R. Albrecht, R.N. Hook H.A. Bushouse (San Francisco), p.159
- Granato G.L. & Danese L., 1994 *MNRAS* 268, 235
- Heckman T.M., Chambers K.C., Postman M., 1992, *ApJ* 391, 39
- Heckman T.M., O'Dea C.P., Baum S.A., Laurikainen E., 1994, *ApJ* 428, 65
- Hes R., Barthel P.D. and Fosbury R.A.E. 1993, *Nat* 362, 326
- Hes R., Barthel P.D. and Hoekstra H., 1995, *A&A* 303, 8
- Hoekstra H., Barthel P.D., Hes R., 1997, *A&A* 319, 757
- Kreysa E., Gemuend H.-P., Gromke J., Haslam C.G., Reichertz L., Haller E.E., Beeman J.W., Hansen V., Sievers A., Zylka R., 1998 Proc. SPIE Vol. 3357, p. 319-325, *Advanced Technology MMW, Radio, and Terahertz Telescopes*, Ed. Thomas G. Phillips
- Ivison R., 1995, *MNRAS* 275, L33
- Ivison R.J., Dunlop J.S., Hughes D.H., Archibald E.N., Stevens J.A., Holland W.S., Robson E.I., Eales S.A., Rawlings S., Dey A., Gear W.K., 1998, *ApJ* 494, 211
- LaValley, M., Isobe, T. and Feigelson, E.D. "ASURV", *Bull. Amer. Astro. Society* 1992
- Lemke D., Klaas U., Abolins J., et al. , 1996 *A&A* 315, L64
- Lilly S.J., Longair M., 1984 *MNRAS* 211, 833
- Lilly S.J. 1989 *ApJ* 340, 77
- McCarthy P. 1993, *Ann.Rev.A&A* 31, 639
- McCarthy P.J., Miley G.K., DeKoff S., Baum S.A., Sparks W.B., Golombek D., Biretta J., Macchetto F., 1997, *A&AS* 112, 415
- Manzini A. & di Serego Alighieri S. 1996, *A&A* 311, 79
- Mazzarella J.M., Graham J.R., Sanders D.B., Djorgovski S., 1993, *ApJ* 409, 170
- Mazzei P., De Zotti G., 1996 *MNRAS* 279, 535
- Meisenheimer K., Haas M., Chini R., Klaas U., Lemke D., 2001, *A&A* 372, 719
- Mirabel I.F., Sanders D.B., Kazès 1989 *ApJ* 340, L9

- Pier E.A., Krolik J. 1992, ApJ 401, 99
- Polletta M., Courvoisier T.J.-L., Hooper E.J. and Wilkes B.J., 2000, A&A 362, 715
- Scarrott S.M, Rolph C., Tadhunter C. 1990, *MNRAS* 240, 5p
- Uson J., Bagri D.S. and Cornwell T.J., 1991, PhysRevLet 67, 3328
- van Bemmell I.M., Barthel P.D., Yun M.S., 1998 *A&AS* 334, 799
- van Bemmell I.M., Barthel P.D., De Graauw T. 2000 *A&AS* 359, 523
- van Bemmell I.M. & Bertoldi F., 2001 *A&AS* 368, 414
- Vernet J., Fosbury R.A.E., Villar-Martín M., Cohen M.H., Cimatti A., di Serego Alighieri S., Goodrich R.W., 2001, A&A, 366, 7
- van den Werf P.P., 1998 in *The most distant radio galaxies*, eds Röttgering H.J.A., Best P.N., Lehnert M.D., Kluwer Academic Publishers (Dordrecht).

Table 1. 1.25 mm Observations of 3C sources

name	redshift	type	Flux (mJy)	stat. uncer. (mJy)	cal. uncer. (mJy)
3C46	0.437	G	<3.6		
3C268.1	0.974	G	4.5	1.2	0.4
3C268.3	0.371	G	4.1	0.8	0.4
3C268.4	1.400	Q	6.1	1.0	0.6
3C277	0.414	G	2.5	1.0	0.2
3C280.0	0.998	G	12.0	1.3	1.2
3C280.1	1.659	Q	3.5	1.4	0.3
3C286.0	0.849	Q	428.0	3.2	40.0
3C287.0	1.055	Q	108.0	1.4	10.0
3C288.1	0.961	Q	4.4	0.9	0.4
3C289.0	0.967	G	3.4	0.9	0.3
3C292.0	0.713	G	3.4	1.1	0.3
3C293.1	0.709	G	< 3.0		
3C295.0	0.461	G	35.6	2.1	4.0
3C305.1	1.132	G	3.4	1.3	0.3
3C309.1	0.905	Q	385.8	2.5	38.0
3C313.0	0.461	G	< 2.7		
3C320.0	0.342	G	3.7	0.8	0.3
3C322.0	1.681	G	< 3.0		
3C323.0	0.679	G	1.9	0.8	0.2
3C325.0	0.860	G	4.3	1.0	0.4
3C337.0	0.635	G	< 3.0		
3C343.0	0.988	Q	6.6	1.6	0.6
3C343.1	0.750	G	8.9	1.4	0.8
3C345.0	0.593	Q	3480.0	40.0	300.0
			2150.0	12.0	100.0
3C352.0	0.806	G	5.8	1.4	0.6
3C356.0	1.079	G	< 3.0		

Uncertainties are given at 1σ levelupper limits at 3σ

Table 2. IRAS Observations of 3C sources

name	12 μm (mJy)	25 μm (mJy)	60 μm (mJy)	100 μm (mJy)
3C46	< 105	< 66	< 141	< 350
3C268.1	< 60	< 60	< 75	< 300
3C268.3	< 80	< 74	< 114	< 345
3C268.4
3C277	< 120	< 100	170 \pm 40	< 450
3C280.0	< 66	< 90	90 \pm 30	< 300
3C280.1	< 90	< 75	< 90	< 390
3C286.0	< 75	< 105	< 90	< 270
3C287.0	< 100	< 120	< 150	< 180
3C288.1	< 75	< 60	< 75	< 180
3C289.0	< 75	70 \pm 20	100 \pm 40	< 210
3C292.0	< 60	< 75	< 90	< 240
3C293.1	< 120	< 180	< 143	< 330
3C295.0	< 30	< 60	< 66	< 210
3C305.1	< 60	< 60	< 60	280 \pm 75
3C309.1	< 75	80 \pm 14	< 120	< 600
3C313.0	< 70	< 90	170 \pm 32	240 \pm 80
3C320.0	< 60	< 66	110 \pm 33	270 \pm 90
3C322.0	< 60	< 45	90 \pm 25	200 \pm 75
3C323.0	< 66	< 54	< 90	< 150
3C325.0	< 60	< 45	< 60	< 180
3C337.0	< 60	< 60	< 80	< 250
3C343.0	< 36	< 45	< 60	< 180
3C343.1	< 45	< 45	< 75	< 450
3C345.0	160 \pm 20	310 \pm 20	700 \pm 30	1140 \pm 70
3C352.0	< 75	< 75	< 100	< 240
3C356.0	< 75	< 75	< 75	< 400
averages RGs	10 \pm 5	< 15	36 \pm 5	59 \pm 30
averages QSOs	27.8 \pm 11	23 \pm 8	29 \pm 8	62.6 \pm 27

averages were computed with
 SUPERSKANPI procedures without 3C345

Table 3. ISO Observations of 3C sources

name	$5\mu m$ (mJy)	$7\mu m$ (mJy)	$12\mu m$ (mJy)	$25\mu m$ (mJy)	$60\mu m$ (mJy)	$90\mu m$ (mJy)	$170\mu m$ (mJy)	$200\mu m$ (mJy)
3C46	<50	<40	<300	<480
3C268.3	<37	...	<84	<41	<180	<500
3C268.4	74 ± 20	430 ± 87	...
3C280.0	<7	<25	<90	< 120	120 ± 40	76 ± 21	<260	...
3C286.0	<10	120 ± 40	100 ± 30
3C287.0	<20	...	<70	...	<120	<100
3C288.1	2.28 ± 0.33^a	...	<180	<136	<190	...
3C295.0	<20	1.41 ± 0.43^a	160 ± 40	140 ± 35	...	<300
3C305.1	1.52 ± 0.30^a
3C309.1	20 ± 8	<30	8.18 ± 0.99^a	...	100 ± 30	<180	<260	...
3C313	<200
3C325.0	<50	<20	<60	...	150 ± 40	100 ± 30	<100	...
3C337.0	<90	<54	<150	<600
3C343.0	1.39 ± 0.27^a
3C343.1	0.80 ± 0.27^a	<120	220 ± 40	<250
3C352.0	<1.2 ^a	<110	135 ± 70	...
3C356.0	0.83 ± 0.28^a	110 ± 65	<70	...

^a ISOCAM data